Article

Improved Model-Free Deadbeat Predictive Current Controller for PMSMs Based on Ultralocal Model and *H*∞ Norm

Yiming Fang and Junlei Chen *

School of Mechanical and Electrical Engineering, Shaoxing University, Shaoxing 312000, China; ymfang@usx.edu.cn
* Correspondence: chenjunlei@seu.edu.com

Abstract: This article proposes an improved model-free deadbeat predictive current control (MFCC) method for permanent magnet synchronous motors (PMSMs) based on the ultralocal model and *H*∞ norm. Firstly, the traditional deadbeat predictive current control (DPCC) method is introduced and a theoretical analysis is conducted on its sensitivity to parameters. Building upon this, the limitations of model dependence and the limited robustness of the deadbeat predictive current control method based on the extended state observer (ESO-DPCC) are theoretically analyzed. Furthermore, an improved MFCC method based on the ultralocal model is proposed, and the influence of the observer on MFCC is theoretically analyzed. This study combined the proposed method with the *H*∞ norm, and the optimal coefficients of the observer were tuned to enhance the robustness and dynamic performance of the current loop. Finally, the proposed algorithms were validated on a 400 W PMSM platform.

Keywords: permanent magnet synchronous motors; deadbeat predictive current control; *H*∞ norm; model free

1. Introduction

1.1. Motivation

Permanent magnet synchronous motors (PMSMs), benefiting from advantages such as high power density, high efficiency, and high dynamic performance, have been widely applied in fields such as robotics and electric vehicles [1,2]. The performance of PMSMs in the above fields relies heavily on the design of high-performance controller algorithms. Among these, the dual-closed-loop control strategy for speed and current, widely used in motor control due to its excellent dynamic and steady-state performance, has continued to be utilized [3]. However, due to the inner loop of the traditional dual-closed-loop control structure, the performance of the current controller directly limits the control performance of the outer speed loop, which is especially crucial for dynamic performance and robustness, particularly in industrial applications such as robots [4]. Therefore, achieving fast and robust current control performance for PMSMs is of great significance for their overall high performance control. Additionally, compared to analog control, whose performance is easily affected by environmental interference, digital control offers flexible controller design and the ease of implementing various high-performance control algorithms. Hence, in this study, digital control was used to design a current control algorithm for PMSMs.

1.2. Related Research

(1) PI Controller: Common current control strategies include the PI controller, model predictive controller, and deadbeat predictive current controller (DPCC). Among them, the traditional PI controller suffers from issues such as *dq*-axis cross-coupling and digital delay. For the cross-coupling issue, common solutions include diagonalization decoupling, disturbance rejection decoupling, and inverse system decoupling techniques [5]. However, although the above algorithms can improve the performance of traditional PI

current controllers, the complexity of the current controller is simultaneously increased. Moreover, the improved PI current controller is still affected by digital delay, resulting in limited bandwidth.

(2) Model Predictive Controller: To address the digital delay issue in the current loop, the most common and effective solution is model predictive control (MPC). Common MPC methods can be divided into finite control set model predictive control (FCS-MPC) [6,7] and continuous control set model predictive control (CCS-MPC) [8]. FCS-MPC selects the optimal voltage vector to achieve current control by designing a cost function to iterate through inverter switch combinations. This algorithm offers faster dynamic performance compared to PI control but suffers from inherent drawbacks such as high computational complexity and torque ripple [9]. Introducing modulation strategies like space vector pulse width modulation effectively suppresses torque ripple and fixes the switching frequency. This approach is similar to CCS-MPC mentioned above; however, CCS-MPC still faces high computational complexity, and both MPCs are sensitive to motor parameters, with control performance strongly dependent on the accuracy of electromagnetic parameters [10].

(3) Deadbeat Predictive Current Controller: Compared to PI current control and MPCs, DPCC has drawn considerable attention due to its advantages of a simple structure and fast dynamic performance [11]. However, similar to MPCs, the model-driven nature of DPCC also makes its response sensitive to models. In addition, a qualitative comparison of the three controllers in terms of dynamic performance, robustness, and algorithm complexity is shown in Table 1. To improve parameter robustness, there are two main approaches: integrating online parameter identification algorithms and adding disturbance observers.

Table 1. Comparison table of different controllers.

	PI Controller	*Model Predictive Controller*	*Deadbeat Predictive Current Controller*
Fast Dynamic Performance	★	★★	★★★
Strong Robustness	★★	★	★
Easy Implementation	★★	★	★★★

Regarding the first approach, its performance often depends on the convergence accuracy and speed of the online parameter identification algorithm. Additionally, in cases where initial parameter errors exist, severe current fluctuations in the DPCC current loop due to errors can adversely affect the convergence performance of the online identification algorithm, making the design and analysis of this approach more complex [12]. For the second approach, the robust control of DPCC is achieved by designing observers to observe and compensate for the aggregated disturbances caused by parameter errors [13,14]. Compared to online parameter identification, this approach still maintains the advantage of a simple structure. Common observers include Internal Model Disturbance Observer, Luenberger Observer, and Linear Extended Observer. ESO maintains current performance in the absence of parameter errors, diminishes steady-state error, enhances robustness in the presence of parameter errors, and ensures stable operation even with a twofold increase in inductance error [15]. However, despite the advantages of observer-based approaches, the design of controllers still requires motor models and parameters, and the design process remains complex. Additionally, traditional pole-placement parameter configuration methods have limited effectiveness in improving robustness.

To further decrease the reliance of current control algorithms on models and parameters, the model-free theory based on intelligent algorithms like neural networks [16,17] and the ultralocal model can be utilized for designing model-free controllers. The ultralocal model, characterized by its simple structure and easy implementation, has been applied in speed control and current control [18]. In speed control applications, the ultralocal model can enhance the robustness of speed loop control and suppress torque ripple [19,20], while, in current control applications, compared to ESO-DPCC, a model-free current controller

only requires the tuning of two parameters: gain and disturbance, instead of four parameters including resistance, inductance, flux linkage, and disturbance. The disturbance can be estimated through an observer [21]. However, the initial values of controller coefficients are often set as the inverse of inductance, indicating that the design process still cannot completely eliminate dependence on the parameter. Although the robustness of the controller to inductance parameters can be improved through adaptive methods for controller coefficients, this method requires additional signal injection, leading to additional electromagnetic interference and high-frequency losses. Additionally, traditional observer parameters are often simplified as overlapping poles, further limiting the robustness of controllers to parameter variations [22].

1.3. Contributions and Organizations

The primary contributions of this article include (1) analyzing the impact of parameter variations on multiple current controllers, (2) enhancing the dynamic performance of the conventional controller based on the ultralocal model, (3) analyzing the influence of ESO coefficients on controller robustness, and (4) proposing an improved ESO coefficient design method for an ultralocal model-based current controller.

Furthermore, the structure of the subsequent sections of this article is organized as follows. A brief introduction to the mathematical model of PMSMs and traditional DPCC is provided in Section 2. Section 3 introduces traditional ESO-based DPCC and the MFCC. Section 4 presents the optimal coefficients selection method for MFCC proposed in this article, and experimental validation is described in Section 5. Finally, Section 6 concludes this article.

2. PMSM Model and Traditional DPCC

2.1. Model of the PMSM

In the continuous domain, the voltage equation of the PMSM in the *dq*-axis can be represented as follows:

$$u_{dq} = (R_s + jL_m\omega_e + L_m p)i_{dq} + j\varphi_m\omega_e \tag{1}$$

where u_{dq} represents *dq*-axis voltages, i_{dq} represents *dq*-axis currents, R_s is the resistance, L_m is the inductance, ω_e is the electrical angular speed, p is the differential operator, and φ_m is permanent magnet flux. Based on the above voltage equation, the current controller can be designed. However, in practical applications, the inherent delay of the control system will affect performance. As shown in Figure 1, the update of PWM occurs at time *k*, and the PWM sequence computed at time *k* needs to be loaded at time *k* + 1, with its corresponding response sampled at time *k* + 2. Therefore, there exists an inherent delay of two cycles. Taking this characteristic into account, the corresponding differential equation for PMSM current is given as follows:

$$i_{dq}(k+1) = \left(1 - \frac{R_s T_s}{L_m} - j\omega_e T_s\right)i_{dq}(k) + \frac{T_s}{L_m}u_{dq}(k-1) - j\frac{\omega_e\varphi_m T_s}{L_m} \tag{2}$$

where *k* designates the control interval and T_s is the control period.
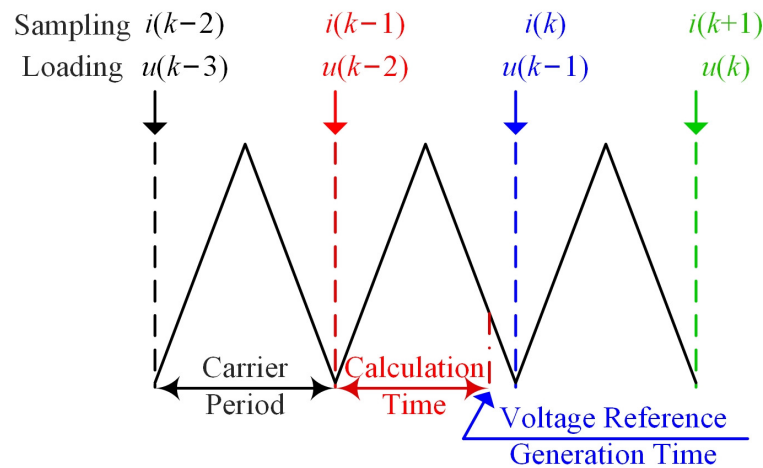
Figure 1. PWM loading characteristic.

2.2. Traditional DPCC

The voltage model of the PMSM considering digital delay is provided above. Building upon this foundation, the conventional DPCC can be formulated as follows:

$$u_{dq}(k) = \frac{L_c}{T_s} i_{dq}(k+2) - \frac{L_c}{T_s}\left(1 - \frac{R_s T_s}{L_c} - j\omega_e T_s\right) i_{dq}(k+1) + j\omega_e \varphi_c \qquad (3)$$

where R_s, L_c, and φ_c are the resistance, inductance, and permanent magnet flux of the controller. To assess the control performance of DPCC, its closed-loop transfer function is given as follows:

$$i_{dq} = \frac{\frac{L_c}{L_m}}{z^2 + \frac{L_c}{L_m}(1 - j\omega_e T_s)^2 - (1 - j\omega_e T_s)^2} i_{dq}(ref) + \frac{\left(z^{-1}\frac{T_s}{L_m}\omega_e^2 T_s + j\frac{2\omega_e T_s}{L_m}\right)}{z^2 + \frac{L_c}{L_m}(1 - j\omega_e T_s)^2 - (1 - j\omega_e T_s)^2}(\varphi_c - \varphi_m) \quad (4)$$

It can be observed that when there is no parameter error in DPCC, it can achieve two-cycle tracking of the reference signal with fast dynamic performance. However, due to its dependence on several motor parameters during the controller design process, parameter errors will affect its performance. Considering that the flux linkage, as shown in (4), does not affect the robustness, the closed-loop pole trajectories of DPCC with different resistance and inductance parameter errors are provided in Figure 2.
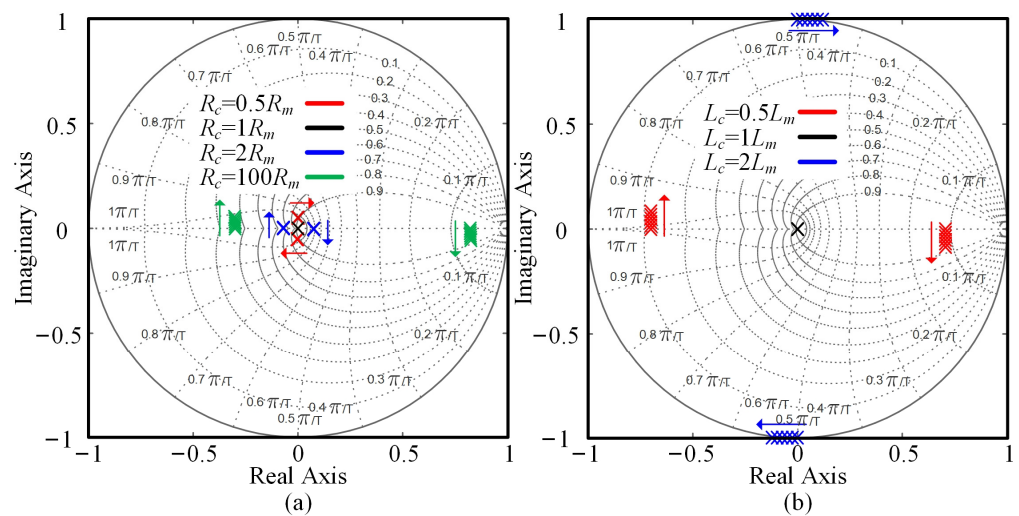

Figure 2. Different parameter ratios result in DPCC closed-loop pole trajectories. (**a**) Resistance. (**b**) Inductance.

It can be observed that when there is no parameter error ($\gamma_R = R_c/R_m = 1$), the two closed-loop poles overlap at the origin, allowing the system to achieve deadbeat performance. With low parameter error ratios ($\gamma_R = 0.5$, $\gamma_R = 2$), the pole positions slightly deviate and exhibit minor movements with increasing speed, with negligible impact. Even in extreme scenarios of almost impossible parameter error ratios ($\gamma_R = 100$), the pole displacement range at rated speed remains within the unit circle, ensuring system stability. Considering that under normal operating conditions, it is unlikely for the winding resistance to vary by more than two times the normal value, the influence of resistance parameters on traditional DPCC is minimal.

Regarding inductance parameters, the system achieves deadbeat performance when there is no parameter error ($\gamma_L = L_c/L_m = 1$). Furthermore, even with twice the parameter error, when the controller parameter is less than the actual inductance parameter ($\gamma_L = 0.5$), the poles deviate from the origin but the system remains stable at rated speed, albeit with affected dynamic performance. Conversely, when the controller parameter is greater than the actual inductance parameter ($\gamma_L = 2$), the system poles are already at the critical stability state at zero speed, and the system becomes unstable as the speed increases. It can be seen that DPCC exhibits low robustness to parameters.

3. Introduction of the MFCC

3.1. Traditional ESO-DPCC

To address the sensitivity of DPCC to parameters, the most common approach is to design an ESO to observe disturbances caused by parameter errors and compensate for them. This aims to improve the robustness of traditional DPCC and reduce steady-state errors. Traditional ESO-DPCC can be designed as follows:

$$u_{dq}(k) = \frac{L_c}{T_s}i_{dq}(\text{ref}) + (R_c - \frac{L_c}{T_s} - j\omega_e L_c)i_{dq}^{pre}(k+1) + j\omega_e\psi_c + f_{dq}(k+1) \tag{5}$$

where $f_{dq}(k+1)$ represents the disturbance caused by parameter errors, $i_{dq}(\text{ref})$ is the current reference, and i_{dq}^{pre} is the current prediction. By comparing (3) and (5), it can be seen that ESO-DPCC adds only one additional compensation term for disturbance to traditional DPCC. Furthermore, in the prediction of the current value at time $k + 1$, ESO-DPCC also considers the influence of disturbances. The ESO used to predict values at time $k + 1$ can be rewritten as follows:

$$
\begin{aligned}
i_{dq}^{pre}(k+1) =& (1 - j\omega_e T_s)i_{dq}(k) + \frac{T_s}{L_c}u_{dq}(k-1) - \frac{T_s}{L_c}f_{dq}(k) - j\frac{T_s\omega_e\psi_c}{L_c} - \beta_1 e(k), \\
f_{dq}(k+1) =& f_{dq}(k) - \beta_2 e(k), \\
e(k) =& i_{dq}(k) - i_{dq}^{pre}(k).
\end{aligned} \tag{6}
$$

where β_1 and β_2 are coefficients of the ESO and e is the current error. To analyze the control performance of ESO-DPCC, the current closed-loop transfer function is also provided. Substituting the predicted current value and disturbance value from (6) into (5) yields the voltage vector reference. Subsequently, substituting it into (2) gives the relationship between the current reference and sampled values. Finally, simplification yields the current closed-loop transfer function of ESO-DPCC as follows:

$$
\begin{aligned}
\frac{i_{dq}}{i_{dq}(\text{ref})} =& \frac{L_c}{L_m} \frac{z^2 - (1+\beta_1)z + \frac{T_s\beta_2}{L_c} + \beta_1}{z^4 + a_1 z^3 + a_2 z^2 + a_3 z}, \\
a_1 =& -\beta_1 - 1, \\
a_2 =& \frac{T_s\beta_2}{L_m} + \beta_1 - \beta_1(\frac{L_c}{L_m} - 1)(1 - j\omega_e T_s) + (\frac{L_c}{L_m} - 1)(1 - j\omega_e T_s)^2, \\
a_3 =& (\frac{L_c}{L_m} - 1)(1 - j\omega_e T_s) \times (\frac{T_s\beta_2}{L_m} + \beta_1 - 1 + j\omega_e T_s).
\end{aligned} \tag{7}
$$

where a_1, a_2, and a_3 are intermediate variables. For ease of analysis, it is common practice to configure the two poles, p_1 and p_2, of the ESO such that they overlap within the unit circle to ensure stability. In this case, the observer coefficients β_1 and β_2 can be expressed as follows:

$$
\begin{aligned}
-1 &< p_{1,2} < 1, \\
\beta_1 &= 2p_{1,2} - 1, \\
\beta_2 &= \frac{L_c}{T_s}\left(p_{1,2}^2 - \beta_1\right).
\end{aligned}
\tag{8}
$$

where p_1 and p_2 are two poles of the observer. Considering that the flux linkage has no effect on robustness and the influence of resistance is negligible, here, only the stability of the system under different inductance errors and different speeds is analyzed. The closed-loop pole trajectory of ESO-DPCC with $p_{1,2} = 0.9$ is shown in Figure 3.
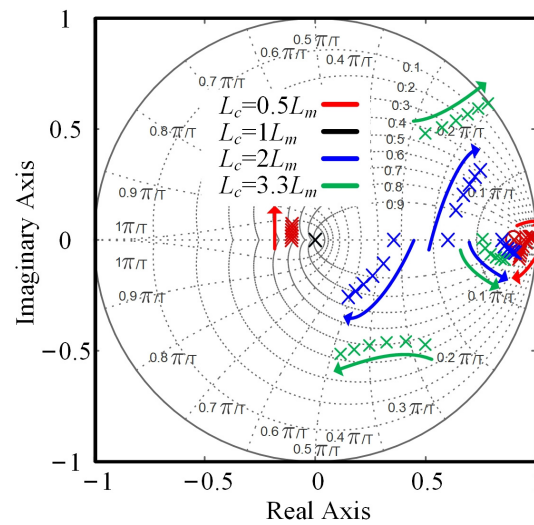

Figure 3. The closed-loop pole trajectories of ESO-DPCC under different inductance ratios.

It can be observed that compared to the results shown in Figure 2 earlier, when the inductance has an error of two times, ESO-DPCC can still ensure that all closed-loop poles are located within the unit circle as the speed increases. However, it is worth noting that the addition of ESO does not infinitely improve robustness. Despite configuring larger pole positions for $p_{1,2}$, when the inductance parameter error further increases to 3.3 times, the poles deviate from the stable boundary at rated speed, and the system becomes unstable. To further enhance the robustness of DPCC and reduce its dependence on motor models and parameters, the following design of model-free DPCC based on the ultralocal model was constructed.

3.2. Model-Free DPCC

(1) Ultralocal Model: For single-input single-output systems, the ultralocal model can be used to describe any unknown complex mathematical model with inputs u and outputs y as $p^v y = a_m u + \varphi$. In this article, for ease of design and analysis, φ is rewritten as $-a_m F$, and the ultralocal model can be rewritten as follows:

$$
p^v y = \alpha_m u - \alpha_m F
\tag{9}
$$

where v is the differential order, u is the input, y is the output, p is the differentiation operator, α_m is the model gain coefficient, and $\varphi = -a_m F$ represents the total unknown disturbance in the model. Furthermore, based on (9), the current differential ultralocal model can be designed as follows:

$$
i_{dq}(k+1) = i_{dq}(k) + \alpha_m T_s u_{dq}(k-1) - \alpha_m T_s F_{dq}(k)
\tag{10}
$$

where F_{dq} represents total disturbances. Comparing (2) and (10), it is easy to see that the coefficient α_m is essentially the reciprocal of L_m, and $F_{dq}(k) = (j\omega_e - R_m/L_m)i_{dq}(k) - j\omega_e\psi_m/L_m$. Furthermore, building on this, MFCC is formulated in the following sections.

(2) Design of MFCC: On the basis of the current differential ultralocal model given in (10), considering the influence of speed, the predictive current controller can be designed as follows:

$$i_{dq}(k+1) = (1 - j\omega_e T_s)i_{dq}(k) + \alpha_m T_s u_{dq}(k-1) - \alpha_m T_s F_{dq}(k) \tag{11}$$

Furthermore, building on this, MFCC can be formulated as follows:

$$u_{dq}(k) = \frac{1}{\alpha_c T_s}[i_{dq}(ref) - (1 - j\omega_e T_s)i_{dq}^{pre}(k+1)] + f_{dq}(k+1) \tag{12}$$

where α_c is gain in the controller. Similar to ESO-DPCC, the predicted current and disturbance terms at time $k + 1$ in MFCC are also observed using ESO. The ESO design in this case is as follows:

$$
\begin{aligned}
i_{dq}^{pre}(k+1) &= (1 - j\omega_e T_s)i_{dq}(k) + \alpha_c T_s u_{dq}(k-1) - \alpha_c T_s f_{dq}(k) - \beta_1 e(k), \\
f_{dq}(k+1) &= f_{dq}(k) - \beta_2 e(k), \\
e(k) &= i_{dq}(k) - i_{dq}^{pre}(k).
\end{aligned}
\tag{13}
$$

Thus, sampling the current at time k, predicting the current and disturbance at time $k + 1$ using the ESO as shown in (13), and substituting them into the controller shown in (12) yields the voltage vector at time k used to achieve deadbeat control. Furthermore, to analyze the control performance of MFCC, the current closed-loop transfer function is given as follows:

$$
\begin{aligned}
\frac{i_{dq}}{i_{dq}(\text{ref})} &= \frac{\alpha_m}{\alpha_c} \frac{z^2 - (1 + \beta_1)z + \alpha_c T_s \beta_2 + \beta_1}{z^4 + a_1 z^3 + a_2 z^2 + a_3 z}, \\
a_1 &= -\beta_1 - 1, \\
a_2 &= (\frac{\alpha_m}{\alpha_c} - 1)(1 - j\omega_e T_s)(1 - j\omega_e T_s - \beta_1) + \alpha_m T_s \beta_2 + \beta_1, \\
a_3 &= (1 - \frac{\alpha_m}{\alpha_c})(1 - j\omega_e T_s)(1 - j\omega_e T_s - \beta_1).
\end{aligned}
\tag{14}
$$

Correspondingly, the closed-loop pole trajectory of MFCC with $p_{1,2} = 0.9$ is shown in Figure 4.
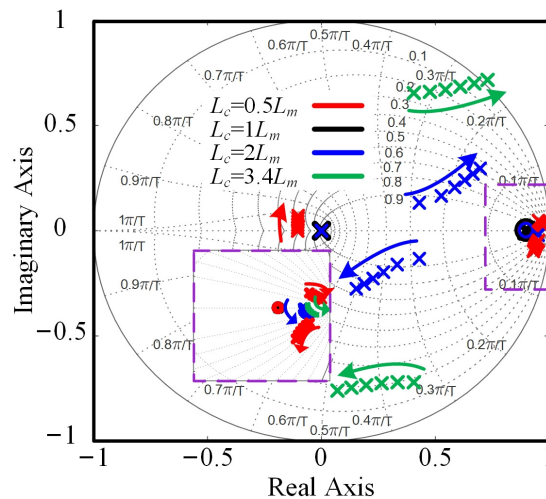

Figure 4. The closed-loop pole trajectories of MFCC under different inductance ratios.

As can be seen, two points of information can be obtained. First, as indicated by the black pole positions, as analyzed above, when the controller coefficients match the ideal model coefficients, the designed MFCC closed-loop poles overlap at the origin and are not affected by changes in speed, proving that MFCC can achieve deadbeat control across the entire speed range. Second, similar to ESO-DPCC, at $\gamma_L = 2$, as the speed increases, the system poles move towards the boundary of the unit circle, until, at $\gamma_L = 3.4$, the system poles move outside the unit circle.

4. *H∞*-Based Coefficient Design

The above analysis indicates that MFCC can enhance robustness without relying on motor models and parameters. However, during the aforementioned design process, the observer coefficients were simplified rather than being the optimal ones. To further improve the robustness of MFCC, a parameter configuration method for MFCC based on *H∞* norm is proposed.

4.1. Influence Analysis of Coefficient on Robustness

Since configuring two observer gains β_1 and β_2 cannot arbitrarily set the poles, it is necessary to optimize the selection of coefficients. Therefore, β_1 and β_2 are selected by solving the optimization equation in this section.

To investigate the influence of observer pole selection on the system, in Figure 4, under the condition of $\gamma_L = 2$ and running at rated speed, the distribution of MFCC closed-loop system poles with different observer poles 0.5, 0.7, 0.9, and 0.95 is shown in Figure 5. The blue dots in the figure represent the original operating conditions shown in Figure 4, where the system remains stable. However, with the change in observer pole position under the same operating conditions, the system poles also change accordingly. As shown by the red and black poles, as the observer pole position decreases, the system bandwidth increases, but the robustness decreases. When the observer pole is configured at 0.5, the system poles move out of the unit stability circle, and the system becomes unstable. As indicated by the green pole, as the observer pole increases to 0.95, system damping decreases and robustness increases. From the above analysis, it can be concluded that the configuration of observer poles significantly affects the bandwidth and robustness of the current loop. Therefore, it is necessary to select the optimal observer pole position.
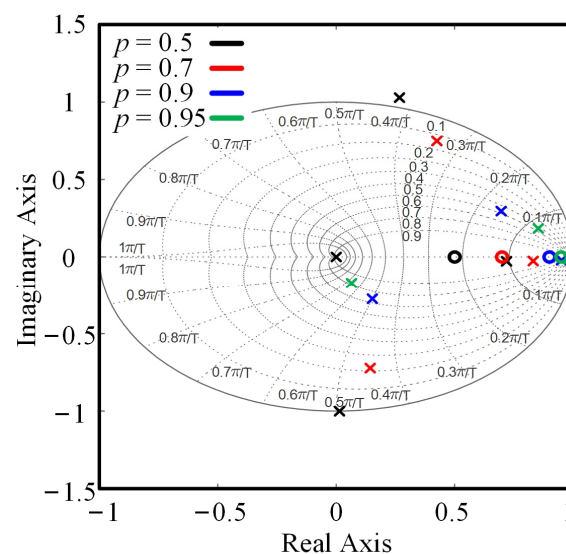

Figure 5. The open-loop pole positions of the current loop under different observer pole locations.

4.2. Coefficient Design

Since the positions of closed-loop system poles are related to system stability and damping, optimizing the closed-loop pole locations is essential. By selecting the observer

gain, the maximum modulus of the closed-loop system poles can be minimized from the origin. This optimization objective ensures that all closed-loop poles remain inside the unit circle while reducing frequency amplification peaks. Additionally, ensuring the stability of the observer allows for the calculation of the restricted range of observer gains as follows:

$$|1 + \beta_1| < 2,$$
$$|\beta_1 + \beta_2 \alpha_c T_s| < 1. \tag{15}$$

Therefore, the optimization equation for selecting the observer gain is expressed as follows:

$$
\begin{aligned}
\min \quad & \max(|pole(f_{clo})|), \\
s.t. \quad & |1 + \beta_1| < 2, |\beta_1 + \beta_2 \alpha_c T_s| < 1, \\
& \max(|pole(f_{clo})|) < 1.
\end{aligned} \tag{16}
$$

where f_{clo} indicates the transfer function (14). According to (16), since it is difficult to obtain an analytical solution for the modulus of the poles of f_{clo}, offline traversal can be directly performed within the feasible domain to obtain the optimal solution for (16). For a single-input single-output system, its $H\infty$ norm represents the maximum peak amplification in the frequency domain. Therefore, in order to quantify the frequency amplification peak under different observer gains, corresponding $H\infty$ parameters are also provided as measures of the amplification peak. Additionally, assuming that the maximum possible system parameter errors are simultaneously present with a twice error in inductance, a 10 times error in resistance, and a twice error in magnetic flux, based on the motor parameters given in Section 5 and substituting them into (16) allows for the calculation of the effects of different observer gains β_1 and β_2 on the $H\infty$ norm and the maximum pole modulus. By solving (16), the optimal parameter settings within the feasible domain can be determined as P_1. To compare the effects of different coefficients on system performance, Table 2 provides three sets of different coefficients.

Table 2. $H\infty$ norm and maximum pole modulus under different coefficients.

	β_1	β_2	$H\infty$	Max($|pole(f_{clo})|$)
P_1	$0.85 - 0.15j$	$0.9 + 0.7j$	2.2257	0.9235
P_2	$0.85 - 0.15j$	$0.15 + 0.2j$	2.1986	0.9913
P_3	0.85	0.50625	3.518	0.9712

Where P_1, P_2, and P_3 are three sets of coefficients. In Table 2, P_1 provides the optimal solution calculated based on (16), where the maximum pole modulus is the minimum value within the feasible domain. P_2 represents the optimal observer gains calculated for the $H\infty$ norm within the feasible domain and P_3 represents the gains calculated with the observer poles fixed at 0.925. Comparing the parameters of P_1 and P_2, their $H\infty$ norms are similar, but there is a significant difference in the maximum pole modulus. To compare the system responses under different pole modulus conditions, the bode plots of P_1, P_2, and P_3 are shown in Figure 6.

From Figure 6, it can be observed that when using the coefficients calculated from optimization, the frequency range at low frequencies is higher than that of P_2 and P_3. Additionally, since the infinity norm of P_1 is greater than that of P_2, its maximum peak amplification in the frequency domain is slightly larger than that of P_2. Therefore, theoretically, it is feasible to select observer coefficients by designing the maximum pole positions. Furthermore, although increasing the observer coefficients can increase the stability margin of the system, allowing the deadbeat controller to operate stably even when the inductance error is doubled, at this point, the frequency response of the system exhibits uncontrollable peaks at high frequencies. This will result in a significant overshoot and a longer transient response in the current step response. However, compared to the traditional method of overlapping poles, the poles configured via the $H\infty$ norm can minimize peaks as much as possible.
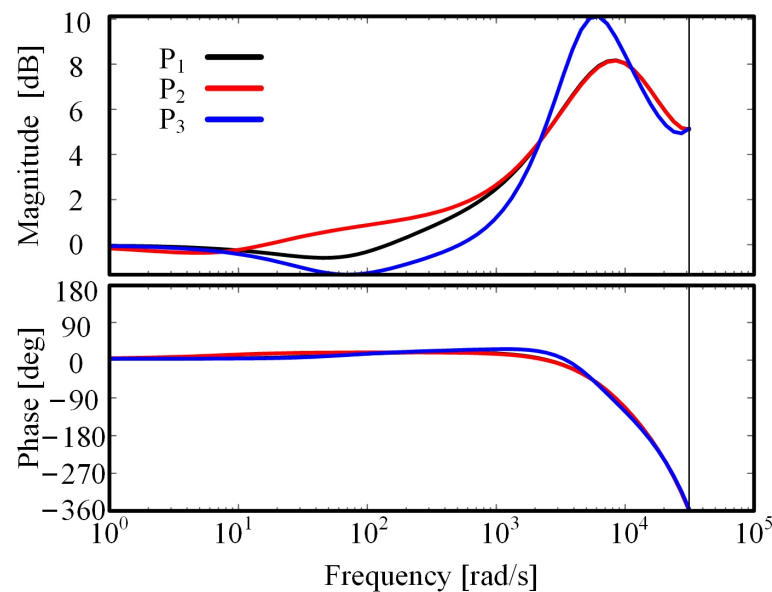
Figure 6. Bode plots of the current closed-loop under different observer coefficients.

As analyzed above, the proposed MFCC based on the ultralocal model and *H*∞ norm can achieve high dynamic and robust control of the PMSM current loop. This aligns with the requirements of motor drivers for industrial robot joints and servo drivers, effectively enhancing the control performance of these drivers.

5. Experimental Verification

5.1. Test Bench Setup

To validate the effectiveness of the above algorithm, this article conducted experiments based on the platform shown in Figure 7, where Figure 7a,b represent the motor platform and controller, respectively. The motor platform in Figure 7a consists of two 400 W PMSM motors with sinusoidal EMF. The main electromagnetic parameters of the test motor were 1.6 Ω, 9 mH, and 0.006 Wb. The encoder used was a TAMAGAWA absolute encoder with a single-turn accuracy of 23 bits and a multi-turn accuracy of 16 bits, meeting the requirements for high-performance positioning and speed measurement. A Sigma-7 motor produced by YASKAWA from Kyushu City, Japan was used for the drag motor, which primarily controlled the speed in this study, focusing on the verification of the current loop performance.

Figure 7b shows the controller, which was designed with integrated driving and sampling circuits. The main power device in the power circuit was an IM513-L6A intelligent power module (IPM) produced by Infineon from Neubiberg, Germany. This IPM adopts the traditional two-level voltage source inverter circuit topology. Additionally, the voltage and current sensors in the experimental platform were LV25-P and LA25-NP, respectively. The MCU employed was a TMS320F28335 chip, and space vector pulse width modulation (SVPWM) was adopted to generate PWM signals with an update frequency of 10 kHz.

When verifying the performance of the current loop control using the aforementioned control platform, the following steps were taken. First, the load motor was operated under a speed model, while the controlled motor was operated with an open-loop speed and closed-loop current model. Second, the voltage and current sensors, along with a position sensor, were used to sample signals, which were then input into the TMS320F28335 via the chip AD7606 produced by ADI from Wilmington, MA, USA. Furthermore, a step current signal was provided, and the proposed current loop was used to generate the reference voltage vector. Finally, SVPWM was employed to generate the corresponding PWM signals to control the inverter and drive the motor.
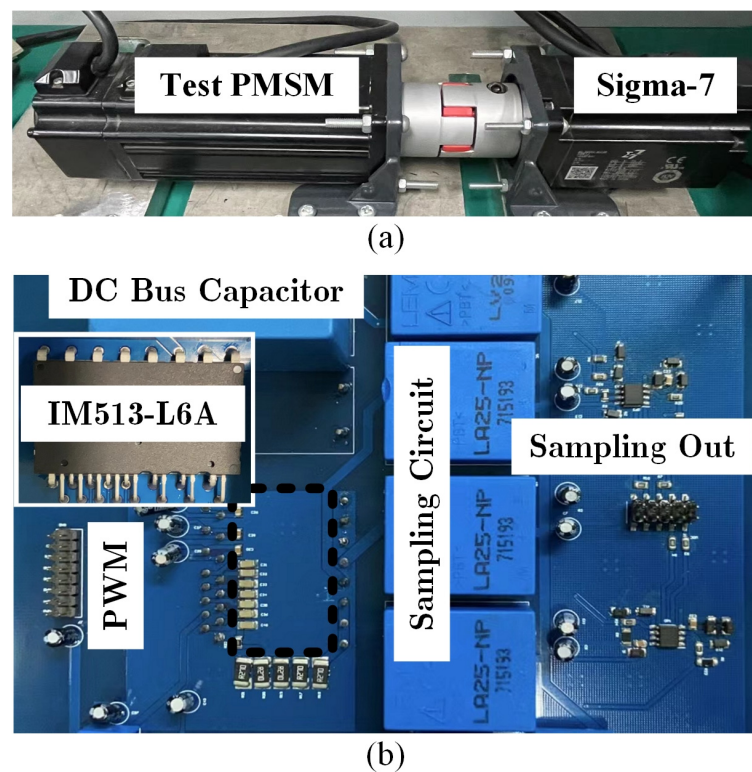
(a)

(b)

Figure 7. Test platform of the PMSM. (**a**) Motor platform. (**b**) Controller.

5.2. Comparative Study

To verify the performance of MFCC, steady and comparative experiments were conducted to compare it with DPCC from multiple aspects. The experimental results are shown in Figures 8–13.

(1) Steady Performance: Before comparing dynamic performance, the steady-state performance of the motor was analyzed. The fast Fourier transform (FFT) results of the steady-state waveforms for the back electromotive force (EMF) and phase current are shown in Figure 8. It can be seen that the back EMF exhibited good sinusoidal quality, with a total harmonic distortion (THD) of only 3.12%. When controlled using the method proposed in this article, the current also exhibited good sinusoidal quality, with a THD of only 6.82%. Additionally, it is worth noting that the fifth harmonic in the current waveform increased to some extent due to the dead-time effect of the switching devices, but the overall impact was minimal.
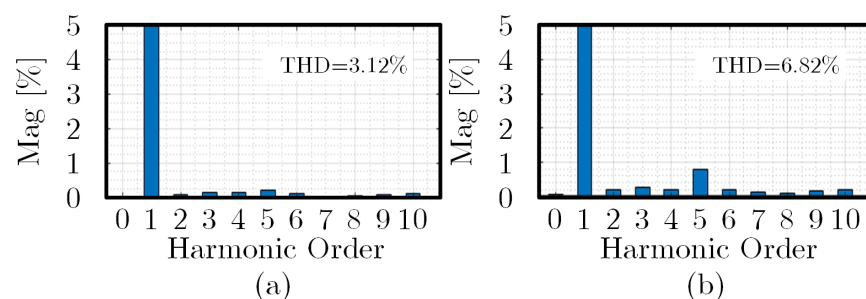
Figure 8. FFT analysis results. (**a**) EMF. (**b**) Phase current.

(2) Comparison of Current Step Responses without Parameter Errors: The current step response comparison between DPCC and MFCC with no parameter errors is presented in Figure 9. It can be observed that without parameter errors, both traditional DPCC and MFCC converged to the reference value after two control cycles, achieving deadbeat

control. In other words, the proposed MFCC maintained its dynamic performance without degradation in the absence of parameter disturbances.
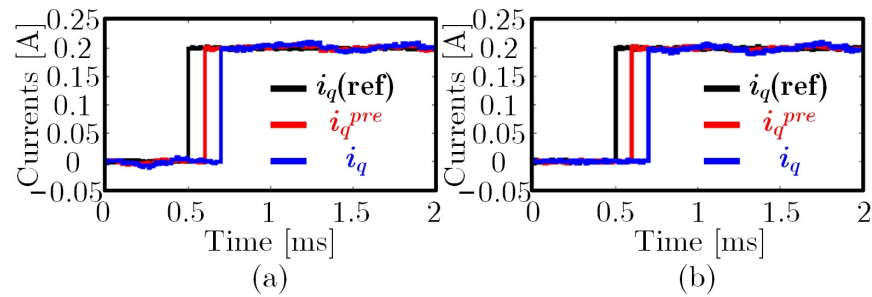

Figure 9. Step response comparison experiment results with no parameter error. (**a**) DPCC. (**b**) MFCC.

(3) Comparison of Current Step Responses with Resistance Error: To verify the robustness of MFCC against resistance parameter disturbances, the experimental comparison results under 10 times resistance error (i.e., $\gamma_R = 10$) are presented in Figure 10. From the results, it can be observed that traditional DPCC was significantly affected by the resistance parameter error, resulting in a noticeable DC bias. As traditional DPCC lacked the means to suppress this bias, it did not converge to zero over time, severely affecting the accuracy of the current control. In contrast, the proposed MFCC, equipped with ESO, effectively suppressed the DC bias disturbance caused by resistance parameter errors. Moreover, due to the relatively small proportion of resistance error, there was no significant adjustment process even in the current response, demonstrating the excellent capability of MFCC in suppressing disturbances caused by resistance parameter errors.
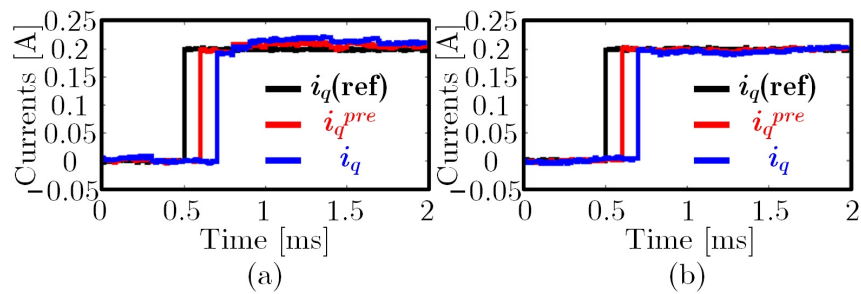

Figure 10. Step response comparison experiment results with $\gamma_R = 10$. (**a**) DPCC. (**b**) MFCC.

(4) Comparison of Current Step Responses with Flux Linkage Error: Furthermore, to verify the capability of suppressing disturbances caused by flux linkage errors, the experimental comparison results under 10 times flux linkage error (i.e., $\gamma_\varphi = \varphi_c / \varphi_m = 10$) are presented in Figure 11. As shown in the figure, similar to the case of resistance parameter error, the presence of flux linkage error led to a noticeable DC bias in the response current. However, since the impact of flux linkage on the current loop was higher than that of resistance, the bias generated in the current was higher than that in the case of resistance error. Similarly, from the experimental results of MFCC, it can be observed that after introducing ESO, the DC bias in the current could be effectively compensated, demonstrating the ability of MFCC to suppress flux linkage bias.
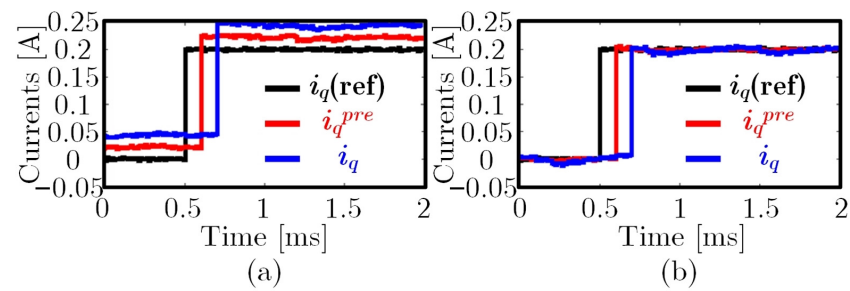
Figure 11. Step response comparison experiment results with $\gamma_\varphi = 10$. (**a**) DPCC. (**b**) MFCC.

(5) Comparison of Current Step Responses with Inductance Error: Moreover, the performance of current response under the disturbance of inductance parameter error was compared. The experimental comparison results are presented for the cases where the controller inductance parameter was smaller or larger than the actual parameter, i.e., $\gamma_L = 0.5$ and $\gamma_L = 2$, as shown in Figure 12. From the results in Figure 12a,b, it can be observed that when the controller parameter was smaller than the actual parameter, this did not affect the robustness of the system. In this case, both traditional DPCC and MFCC converged to the desired current after several cycles of adjustment. However, from the results in Figure 12c,d, it can be seen that when the control parameter was larger than the actual parameter, traditional DPCC lost stability due to its limited robustness, resulting in severe oscillations in the actual current. In contrast, the proposed MFCC, due to its enhanced robustness without compromising dynamic performance, could still converge to a steady state after several cycles of adjustment even with inductance error, demonstrating the stronger robustness of MFCC.
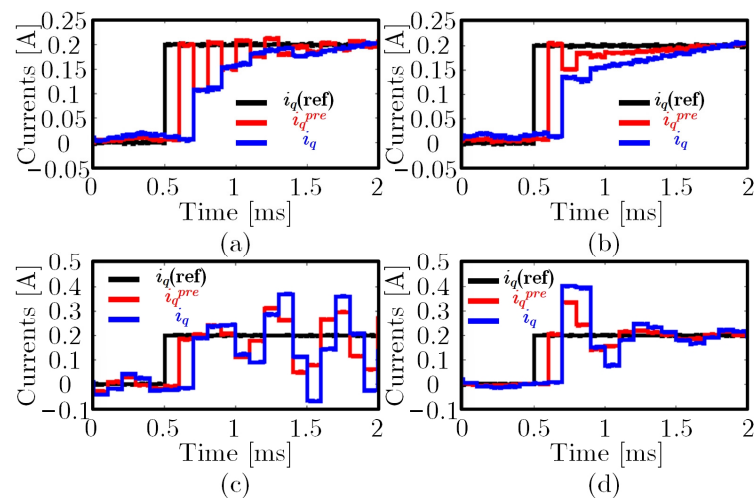

Figure 12. Step response comparison experiment results with $\gamma_L = 0.5$ and $\gamma_L = 2$. (**a**) DPCC, $\gamma_L = 0.5$. (**b**) MFCC, $\gamma_L = 0.5$. (**c**) DPCC, $\gamma_L = 2$. (**d**) MFCC, $\gamma_L = 2$.

(6) Comparison of Current Step Responses with Different Observer Parameters: Finally, the current step response performance of MFCC under different observer parameters was compared. The experimental results are shown in Figure 13, where Figure 13a,b present the results for two sets of parameters, P_1 and P_3, from Table 1, with parameter errors $\gamma_L = 2$ and $\gamma_L = 2.5$. From Figure 13a,b, it can be observed that compared to the tuning based on overlapping poles P_3, the current step response with the optimized tuning based on $H\infty$ norm P_1 exhibited a smaller overshoot and shorter settling time, demonstrating superior performance and validating the theoretical analysis in Figure 6. Additionally, from Figure 13c,d, it can be seen that the ultimate robustness under the tuning of overlapping poles was lower, with the system becoming unstable when the parameter error increased to 2.5. In contrast, for the tuning based on the $H\infty$ norm P_1, the system could still maintain

stability under the same conditions, with only a slight increase in overshoot compared to the case of twice inductance error, demonstrating good robustness and dynamic performance and confirming the effectiveness and correctness of tuning the MFCC parameters based on the $H\infty$ norm.
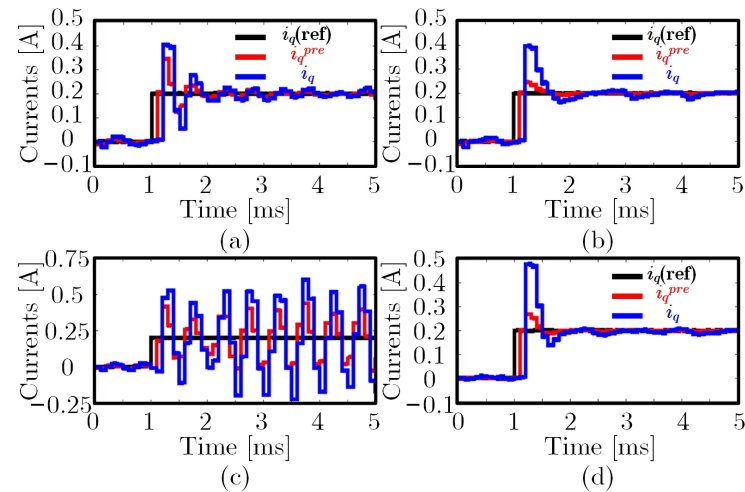

Figure 13. Step response comparison experiment results with k_L = 2 and k_L = 2.5 during different coefficients. (**a**) P_3, γ_L = 2. (**b**) P_1, γ_L = 2. (**c**) P_3, γ_L = 2.5. (**d**) P_1, γ_L = 2.5.

6. Conclusions

This article presented an improved MFCC method leveraging the ultralocal model and $H\infty$ norm. Building upon the analysis of the performance and limitations of traditional DPCC and ESO-DPCC, MFCC was proposed based on the ultralocal model, enabling model-free deadbeat current control without reliance on motor models and parameters, significantly enhancing robustness. Furthermore, addressing the issues of reduced dynamic performance and low robustness limits in the presence of parameter disturbances, a coefficient selection method based on the $H\infty$ norm was proposed, aiming to improve dynamic performance and robustness without altering the controller structure. Finally, the proposed algorithms were validated on a 400 W PMSM experimental platform.

References

1. Li, X.; Wei, Z.; Zhao, Y.; Wang, X.; Hua, W. Design and Analysis of Surface-Mounted Permanent-Magnet Field-Modulation Machine for Achieving High Power Factor. *IEEE Trans. Ind. Electron.* **2024**, *71*, 4375–4386. [CrossRef]
2. Li, X.; Wang, X.; Dong, Y.; Lu, K.; Feng, X. Design and Analysis of Electric-Excitation Claw-Pole Field-Modulated Machine Considering Effective Harmonics. *IEEE Trans. Ind. Appl.* **2024**, *60*, 3893–3902. [CrossRef]
3. Jia, S.; Chen, P.; Yang, D.; Feng, S.; Liang, D. Field Orientation Control for a Dual Winding Dual Magnet Flux Modulated Machine With Torque Distribution Capability. *IEEE Trans. Ind. Appl.* **2024**, *60*, 343–352. [CrossRef]
4. Chen, J.; Fan, Y.; Cheng, M.; Zhang, Q.; Chen, Q. Parameter-Free Ultralocal Model-Based Deadbeat Predictive Current Control for PMVMs Using Finite-Time Gradient Method. *IEEE Trans. Ind. Electron.* **2024**, *70*, 5549–5559. [CrossRef]
5. Hussain, H.A. Tuning and Performance Evaluation of 2DOF PI Current Controllers for PMSM Drives. *IEEE Trans. Transp. Electr.* **2021**, *7*, 1401–1414. [CrossRef]

6. Lu, K.; Li, X.; Zhao, Y.; Yi, P.; Yan, B.; Hua, W. A Novel Three-Vector-Based Model Predictive Flux Control with Low Computation Complexity for SPMSM. *IEEE Trans. Transp. Electr.* **2024**. [CrossRef]

7. Gao, J.; Gong, C.; Li, W.; Liu, J. Novel Compensation Strategy for Calculation Delay of Finite Control Set Model Predictive Current Control in PMSM. *IEEE Trans. Ind. Electron.* **2020**, *67*, 5816–5819. [CrossRef]

8. Zhang, Y.; Yang, H. Two-Vector-Based Model Predictive Torque Control Without Weighting Factors for Induction Motor Drives. *IEEE Trans. Power Electr.* **2016**, *31*, 1381–1390. [CrossRef]

9. Monfared, K.K.; Iman-Eini, H.; Neyshabouri, Y.; Liserre, M. Model Predictive Control With Reduced Common-Mode Voltage Based on Optimal Switching Sequences for Nested Neutral Point Clamped Inverter. *IEEE Trans. Ind. Electron.* **2024**, *71*, 27–38. [CrossRef]

10. Siami, M.; Khaburi, D.A.; Rodríguez, J. Torque Ripple Reduction of Predictive Torque Control for PMSM Drives With Parameter Mismatch. *IEEE Trans. Power Electr.* **2017**, *32*, 7160–7168. [CrossRef]

11. Zhang, X.; Wang, Z.; Bai, H. Sliding-Mode-Based Deadbeat Predictive Current Control for PMSM Drives. *IEEE J. Emerg. Select Top. Power Electron.* **2023**, *11*, 962–969. [CrossRef]

12. Wang, Y.; Liao, W.; Huang, S.; Zhang, J.; Yang, M.; Li, C.; Huang, S. A Robust DPCC for IPMSM Based on a Full Parameter Identification Method. *IEEE Trans. Ind. Electron.* **2023**, *70*, 7695–7705. [CrossRef]

13. Xia, C.; Wang, M.; Song, Z.; Liu, T. Robust Model Predictive Current Control of Three-Phase Voltage Source PWM Rectifier with Online Disturbance Observation. *IEEE Trans. Ind. Inform.* **2012**, *8*, 459–471. [CrossRef]

14. Sun, X.; Lin, X.; Guo, D.; Lei, G.; Yao, M. Improved Deadbeat Predictive Current Control With Extended State Observer for Dual Three-Phase PMSMs. *IEEE Trans. Power Electr.* **2024**, *39*, 6769–6782. [CrossRef]

15. Zhang, Q.; Fan, Y.; Mao, C. A Gain Design Method for a Linear Extended State Observers to Improve Robustness of Deadbeat Control. *IEEE Trans. Energy Convers.* **2020**, *35*, 2231–2239. [CrossRef]

16. Chen, W.; Liu, J.; Fang, Y.; Zhao, J. Timber Knot Detector with Low False-Positive Results by Integrating an Overlapping Bounding Box Filter with Faster R-CNN Algorithm. *Bioresources* **2023**, *18*, 4964–4976. [CrossRef]

17. Fang, Y.; Guo, X.; Chen, K.; Zhou, Z.; Ye, Q. Accurate and Automated Detection of Surface Knots on Sawn Timbers Using YOLO-V5 Model. *Bioresources* **2021**, *16*, 5390–5406. [CrossRef]

18. Fliess, M.; Join, C. Model-Free Control. *Int. J. Control.* **2013**, *86*, 2228–2252. [CrossRef]

19. Zhao, K.; Liu, W.; Zhou, R.; Dai, W.; Wu, S.; Qiu, P.; Yin, Y.; Jia, N.; Yi, J.; Huang, G. Model-Free Fast Integral Terminal Sliding-Mode Control Method based on Improved Fast Terminal Sliding-Mode Observer for PMSM with Unknown Disturbances. *ISA Trans.* **2023**, *143*, 572–581. [CrossRef] [PubMed]

20. Sun, Z.; Deng, Y.; Wang, J.; Li, H.; Cao, H. Improved Cascaded Model-Free Predictive Speed Control for PMSM Speed Ripple Minimization based on Ultra-local Model. *ISA Trans.* **2023**, *143*, 666–677. [CrossRef]

21. Mousavi, M.S.; Davari, S.A.; Nekoukar, V.; Garcia, C.; Rodriguez, J. A Robust Torque and Flux Prediction Model by a Modified Disturbance Rejection Method for Finite-Set Model-Predictive Control of Induction Motor. *IEEE Trans. Power Electr.* **2021**, *36*, 9322–9333. [CrossRef]

22. Zhang, Y.; Jin, J.; Huang, L. Model-Free Predictive Current Control of PMSM Drives Based on Extended State Observer Using Ultralocal Model. *IEEE Trans. Ind. Electron.* **2021**, *68*, 993–1003. [CrossRef]